(*From the* QUARTERLY JOURNAL OF THE ROYAL METEOROLOGICAL SOCIETY, Vol. 106, No. 447, January 1980)

Quart. J. R. Met. Soc. (1980), **106**, pp. 29–56

551.515.127 : 551.515.827 : 551.574.1

Microphysics and dynamics of clouds associated with mesoscale rainbands in extratropical cyclones

By THOMAS J. MATEJKA, ROBERT A. HOUZE, Jr and PETER V. HOBBS

Department of Atmospheric Sciences, University of Washington, Seattle, Washington 98195

(Received 17 January 1979; revised 22 May 1979)

SUMMARY

Measurements obtained with research aircraft in clouds associated with various types of mesoscale rainbands in extratropical cyclones have been examined together with radar data and other detailed measurements. The analyses have yielded information on the structure and microphysical characteristics of the clouds and the nature of the vertical air motions in the clouds associated with each type of mesoscale rainband, and schematic models of the different mesoscale rainbands have been constructed.

In clouds accompanying warm frontal rainbands, ice particles formed above the warm front, probably in shallow convective cells, and fell into the stable air mass below, where they grew by aggregation and helped glaciate stratiform clouds.

Warm sector rainbands resembled squall lines. A younger, convectively active rainband occurred just ahead of an older, less convectively active one. The younger rainband contained both cloud liquid water and ice particles, and ice particles were growing by riming. The older rainband was nearly glaciated, with ice particles growing by aggregation.

Narrow cold frontal rainbands were located along the convergence lines at the advancing edges of cold frontal zones. Each was associated with a convective updraught, 1 to 5 km wide and 1 to 3 $m s^{-1}$ in magnitude, and a similarly narrow downdraught. The core of the updraught contained young, developing cloud, with much higher cloud liquid water content and lower ice particle concentration than in its immediate surroundings. Ice particles grew by aggregation and were heavily rimed. Wide cold frontal rainbands (several tens of kilometres in width) occurred when lifting above a cold front was enhanced to several tens of centimetres per second. Clouds in this region consisted of supercooled water and ice and contained embedded convective elements. Below the cold front, high concentrations of ice particles grew by aggregation.

Prefrontal surges of cool and dry air occurred above the warm front and ahead of the cold front in occluded cyclones. A surge rainband, resembling a wide cold frontal rainband, occurred at the leading edge of the surge and was followed by a field of convective elements. These elements, sometimes arranged in lines, were in various stages of development.

Postfrontal rainbands were lines of convective clouds located well behind a cold front. They may have been associated with secondary fronts and sometimes appeared to behave as organized convective systems.

1. INTRODUCTION

The classical models of fronts (Bjerknes 1919; Bjerknes and Solberg 1922) still provide invaluable aid in depicting the larger-scale aspects of the formation of clouds and precipitation in extratropical cyclones. However, it is now recognized that precipitation is often produced on scales much smaller than those of cyclonic and frontal circulations (Browning 1974; Harrold and Austin 1974; Houze *et al.* 1976a; Hobbs 1978a). Consequently, to understand how clouds and precipitation develop in extratropical cyclones, it is necessary to investigate the organization of cloud microphysical and dynamical processes on the mesoscale.

Studies of the size and motion of mesoscale precipitation features and the patterns in which they occur within extratropical cyclones (Austin 1960; Austin and Houze 1972; Harrold 1973; Houze *et al.* 1976a; Hobbs and Locatelli 1978) have shown not only that mesoscale organization of precipitation can exist in all regions of the cyclone, but also that mesoscale precipitation features exhibit a hierarchical structure and occur in preferred configurations. Viewed on horizontal maps, larger mesoscale features (having areas of 10^3–$10^4 km^2$) are usually band-shaped and oriented parallel to one of the fronts of the

cyclone. These larger features typically contain smaller areas (up to $10^3 km^2$) of more intense precipitation, which may themselves be band-shaped or irregular.

It has been found that the distribution of variously oriented mesoscale bands of precipitation (called 'rainbands') throughout extratropical cyclones forms a reasonably consistent picture, and Houze *et al.* (1976a) have accordingly devised a system of classifying the rainbands based on their positions and orientations with respect to the fronts. A refined version of their classification is presented in Fig. 1. In addition to some renumbering of the types of rainbands, the present classification incorporates the following changes from the earlier scheme: warm frontal rainbands, types 1a and 1b, are now differentiated by their position, ahead of or coincident with the surface warm front, respectively. The surge rainband, type 4a, which occurs in advance of the cold front in an occlusion, has been added. The rainbands, type 4b, following the surge rainband are an example of the small wave-like rainbands described by Houze *et al.* (1976a).

In this paper we examine aircraft measurements collected within and around mesoscale rainbands of the types depicted in Fig. 1. The airborne measurements are examined in conjunction with data from radars, rawinsondes and other sources to determine insofar as possible: (1) the microphysical structure of the clouds associated with each type of rainband; (2) the nature of the vertical air motions in the clouds associated with each type of rainband; and (3) the relationship of the observed cloud structure to fronts and air masses.

This work extends the purely morphological rainband classification of Houze *et al.*

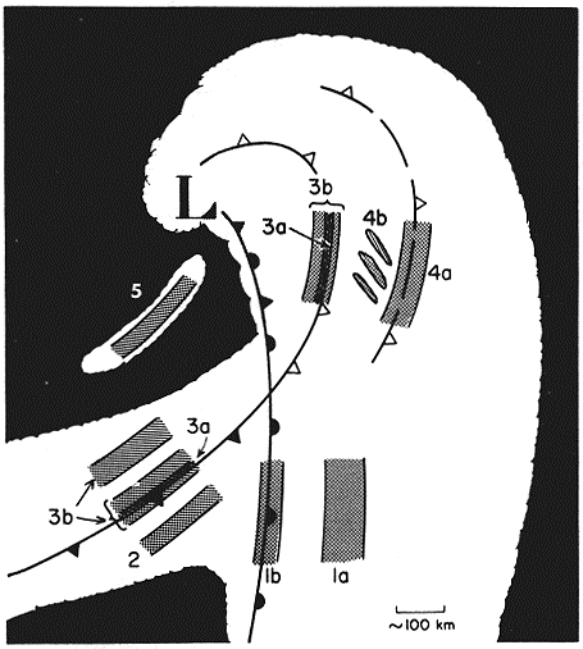

Figure 1. Schematic depiction of the types of mesoscale rainbands (darkly stippled areas) observed in extratropical cyclones. The upper-level cloud shield of the cyclone is shown as white; lower cloud decks are shaded light gray. Type 1: Warm frontal rainbands, of which type 1a occurs ahead of and parallel to the surface warm front, while type 1b coincides with the surface warm front. Type 2: Warm sector rainbands, which occur parallel to and ahead of the surface cold front. Type 3: Cold frontal rainbands, of which type 3a is very narrow and coincides with the cold frontal passage, while type 3b is wider and may straddle the narrow cold frontal rainband or lag behind it. Type 4: The surge rainband, type 4a, coincides with the leading edge of a surge of cold air aloft, ahead of the main cold front in the occluded portion of the cyclone. A field of convection, frequently organized in small rainbands, type 4b, occurs behind the surge rainband. Type 5: Postfrontal rainbands, which occur in the cold air mass to the rear of and parallel to the cold front and usually to the rear of the large cirrus shield associated with the cyclone.

(1976a) in two ways. Firstly, it three-dimensionalizes the previous classification by leading to vertical cross-sections through each of the rainband types depicted horizontally in Fig. 1. Secondly, it identifies physical and dynamical processes associated with the development of precipitation in each type of rainband. The aircraft measurements provide fields of cloud liquid water content, ice particle concentration and ice particle type, which, when mapped in the vertical cross-sections together with thermodynamical data, air motion measurements, radar data and visual cloud observations, provide a basis for synthesizing broad aspects of the precipitation processes in the clouds associated with each type of rainband. It is shown in these syntheses that the development of precipitation in the different types of rainbands shown in Fig. 1 has both distinct differences and important similarities from one type of rainband to another.

2. Data collection

The data described here were obtained as part of the University of Washington's CYCLES (cyclonic extratropical storms) project. A map of western Washington depicting the data-collection networks during the winters of 1974/5 and 1975/6 is shown in Fig. 2. The field programme was conducted in the low-lying, broad Chehalis River valley and Puget Sound basin, away from the Olympic Mountains and Cascade Range. The winds from 950 mb upwards were nearly always between westerly and southwesterly in the storms investigated.

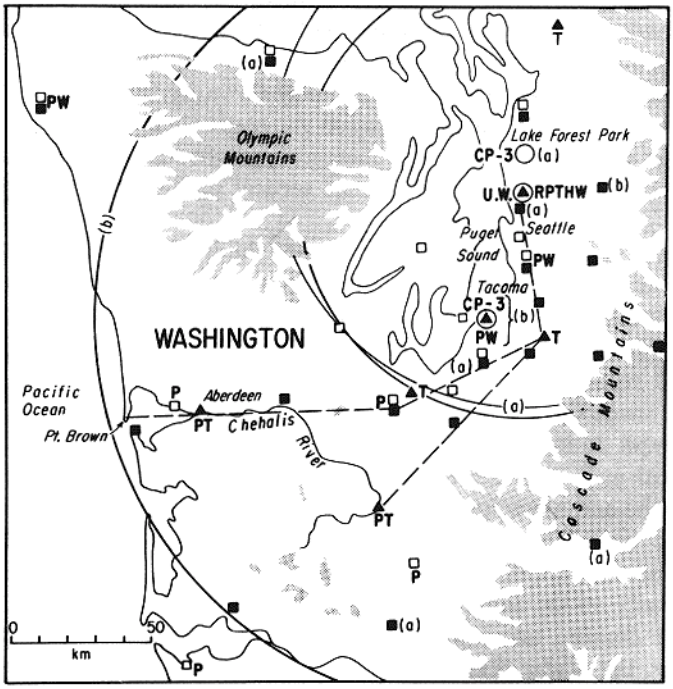

Figure 2. Map of western Washington showing the data-collection networks for the CYCLES project during the winters of 1974–5 and 1975–6. Land areas higher than 600 m above sea level are shaded. Tipping bucket precipitation gauges are indicated by black triangles, weighing bucket gauges by black squares. Airport weather stations are designated by open squares. Rawinsondes were launched from the site indicated by R. Continuous records of surface pressure, temperature, humidity and wind were made at sites designated P, T, H, and W. Dashed lines indicate the paths flown by the two research aircraft. Locations of the University of Washington radars (UW) and the CP-3 radar are shown by small circles; segments of large circles denote their maximum ranges. Items in the network labelled (a) were present only during the winter of 1974–5, items labelled (b) only during the winter of 1975–6.

Orographic effects were consequently mainly to the east and north of our data network. Measurements were made with rawinsondes, surface instruments, weather satellites, a network of precipitation gauges, three radars, and two cloud physics research aircraft. The characteristics and scanning procedures of the three radars are given in Table 1.

TABLE 1. CHARACTERISTICS AND SCANNING PROCEDURES OF WEATHER RADARS USED IN THE CYCLES PROJECT

Radar	UW* surveillance	UW* pulsed Doppler	NCAR† CP-3 Doppler
Wavelength (cm)	3·2	3·2	5·45
Beamwidth (°)	1	0·5	1
Peak power (kW)	250	7	338
Scanning procedure	PPI scans at 0·5° elevation	Vertically pointing	PPI scans at 11 elevation angles from 0 to 20°; some vertically pointing and RHI scans

*University of Washington.
†National Center for Atmospheric Research.

The airborne measurements consisted of thermodynamical, dynamical and microphysical measurements and were obtained with the University of Washington's (UW) converted Douglas B-23 research aircraft and with the National Center for Atmospheric Research's Sabreliner aircraft. The paths normally flown by the aircraft, shown in Fig. 2, were situated over the heart of the precipitation gauge network. The aircraft flew horizontal traverses, often at several levels, through mesoscale rainbands which lay across one of the flight paths. During the winter of 1974/5 some vertical profiles over tipping-bucket gauges were also flown.

Microphysical parameters measured on board the B-23 aircraft included cloud liquid water contents and ice particle concentrations. Sizes and habits of ice crystals and the degrees to which ice particles were rimed and aggregated were determined from replications of the hydrometeors in formvar and from impressions of the hydrometeors made by impaction onto foil. Visual records of the cloud configurations encountered by the B-23 along its flight paths were made by means of photography and by sketches drawn by an observer on a time–height graph during each flight.

Microphysical measurements were made on the Sabreliner with a particle measuring system cloud probe and a precipitation probe (Knollenberg 1970; Heymsfield 1976). These probes measured the sizes and concentrations of particles in the size range 0·03 to 0·38 mm. Examples of these data are described by Houze *et al.* (1979). Cloud photography was employed continuously on the Sabreliner during daylight hours.

For a more detailed account of the facilities and their modes of operation in the CYCLES project, the reader is referred to Hobbs (1978b).

3. ANALYTICAL TECHNIQUES

(*a*) *Use of microphysical data*

The microphysical data obtained in this study were not isolated spot measurements. Rather, they were obtained along extensive flight paths running back and forth at various altitudes through the clouds associated with well-defined mesoscale rainbands. From these

data, the patterns of microphysical parameters over large regions of clouds associated with the rainbands could be constructed. The spatial distributions of cloud liquid water contents, ice particle concentrations, ice crystal habits, and the degrees to which ice particles were rimed and aggregated indicate not only the microphysical mechanisms of precipitation growth in the clouds associated with the rainbands, but also aspects of the mesoscale structures and dynamics of the clouds. Mesoscale structure is indicated by the spatial variation in cloud composition seen in the pattern of the microphysical parameters. Aspects of cloud dynamics are inferred from the microphysical parameters in the following ways:

1. The presence of supercooled cloud water implies the presence of ascending air producing new cloud droplets. This inference is particularly applicable if frozen precipitation was also present in that region of the cloud, for ascent was then necessary to maintain the presence of the supercooled water.

2. A region of glaciated cloud at temperatures well above $-40°C$ indicates that ascending air motions either were not present or were so weak that measurable concentration of droplets could not be maintained in the presence of the ice.

3. Ice crystal habits observed from the aircraft indicate the air temperatures at which the ice particles were nucleated and grew by deposition of vapour. If these temperatures were similar to the temperature at flight level, it is inferred that upward air motion was occurring at this altitude with sufficient magnitude and persistence to continue to produce new ice crystals. If the nucleation temperatures of the observed crystals were lower than the temperature at the flight altitude, it is concluded that the lifting needed to generate the ice particles was occurring at some higher level, and that ascending air motions at and above flight level were sufficiently weak to allow the ice particles to drift downwards.

4. Riming on ice crystals indicates that the crystals had been in a region characterized by a considerable amount of supercooled cloud water and, most likely, of strongly ascending air motions. Heavy riming and graupel, in particular, are typically associated with strong convective updraughts.

5. The relative amounts of liquid water and ice in clouds can indicate the age of a cloud. Supercooled droplets appear alone in the early stage of a cloud's development; a cloud then evolves with both liquid and ice present; finally, glaciation occurs.

(*b*) *Determination of coordinate systems relative to rainbands*

In order to examine measurements made on board the B-23 and Sabreliner aircraft as they flew through the clouds associated with mesoscale rainbands, data along the paths of the aircraft are displayed in cross-sections constructed by projecting the data onto vertical planes oriented perpendicular to and moving with the rainbands. The usefulness of this procedure, of course, depends on cross-band variations being generally strong enough to be identifiable even though significant variability exists along the rainband as well. We find the technique to be quite satisfactory, probably because variability along the band tends to be of random nature, while trends across bands are systematically similar.

In order to plot the data in vertical cross-sections, it was necessary to know the locations of both the aircraft and the rainbands as functions of time. Positions of the aircraft were recorded by navigational equipment on the aircraft every 2 min (corresponding to about 7 km of flight) for the B-23 and every minute (corresponding to about 8 km of flight) for the Sabreliner. Since the flight paths were generally restricted to straight line segments, accurate interpolation between these recorded positions was possible. Tracking of the rainbands across the region where the aircraft flew was accomplished primarily with raingauge data for the winter of 1974/5, and with both raingauge and CP-3 radar data for subsequent winters. The procedure by which the rainbands were identified and tracked is

described in steps 1 and 2 below, while steps 3 to 6 describe how the coordinate axes oriented perpendicular to and moving with the rainbands were determined and used to incorporate data into vertical cross-sections.

Step 1: Identifying the rainbands. Movies of PPI displays from the UW's search radar were reviewed in conjunction with the precipitation record at the UW to obtain a tabulation of the mesoscale precipitation features that occurred at this site in the storms. The passage of a mesoscale echo at the UW was related to records of surface pressure, temperature and wind, and any special behaviour in these parameters associated with the mesoscale precipitation feature was noted.

Step 2: Tracking the rainbands. The precipitation features were then tracked backwards and forwards across the rest of the network by using data from the raingauges and radars and by comparing the various available records or observations of pressure, temperature and wind to aid in identifying a mesoscale precipitation feature with that observed at UW. Of the large mesoscale rainbands thus identified, only those across which the aircraft flew are included in this study.

Step 3: Establishing the orientation of the S axis. The orientation of a horizontal S axis perpendicular to the length of a rainband (Fig. 3(a)) was established from the times of the passage of the front and back edges of the rainband at raingauge sites throughout the network. In this step, each edge of the rainband was assumed, temporarily, to be a straight line that moved at a constant speed across the network. For each of the two lines, corresponding to the two edges of the rainband, there were found an orientation, an initial position, and a speed that produced the least-squares error in timing at the sites in the network. The orientations of the front edge and back edge determined in this way never differed by more than a few degrees for any rainband, and the orientation of the rainband was assumed to be the average of these two calculated orientations. The S axis was directed normal to this orientation. Confidence in the analyses and tracking of the mesoscale rainbands from raingauge to raingauge was given by the small (only a few minutes) root-mean-square differences in the timings produced in these determinations of the orientations of the rainbands.

Step 4: Determining the motion of a rainband along the S axis. Once the orientation of the S axis was established for a rainband, the assumption that the edges of the rainband be straight lines moving at constant speeds was relaxed. Since the primary purpose of this analysis was to position aircraft observations accurately ahead of, within, or behind the moving band of precipitation, only stations along or in the vicinity of the paths flown by the aircraft (e.g. stations A, B, C, D and E in Fig. 3(a)) were used to determine the motions of the edges of the rainband along the S axis. The durations of the rainband over each of these stations, determined in steps 2 and 3, were plotted in an S–time plot (Fig. 3(b)), and the progress of the leading and back edges of the rainband in the S direction were obtained by connecting the edges of the rainband in this S–time plot.

Step 5: Positioning the aircraft relative to a rainband. The path of the aircraft was also plotted in the S–time plot. For each position of the aircraft, the time interval, τ, between the aircraft's occupation of that position and the rainband's arrival at that location was obtained from the S–time plot, as shown in Fig. 3(b). (*Time* from the rainband was chosen as the coordinate relating the aircraft and the rainband rather than *distance* from the rainband, because, for every position occupied by the aircraft, the time when the rainband arrived there was known, while, during the flight, the position of the rainband was not always known.) Because a rainband would sometimes change in width as it progressed across the network, the following method was used to normalize the aircraft's timings relative to the rainband for successive penetrations: If the aircraft was positioned ahead of the rainband, τ was taken simply to be the time remaining before the leading edge of the rainband arrived

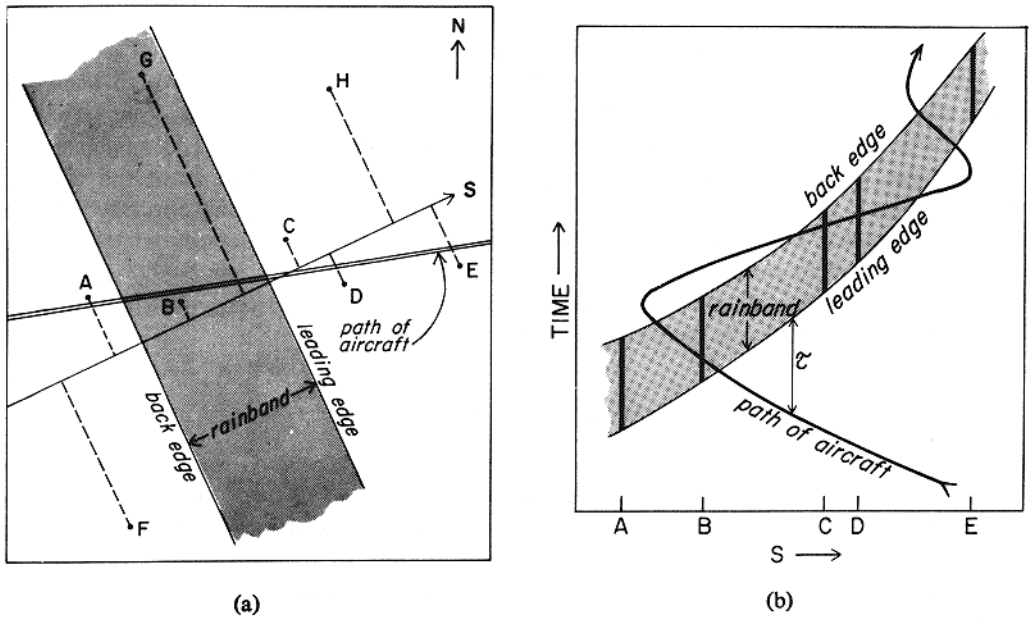

Figure 3. Illustration of two steps in the method by which the research aircraft were positioned relative to a mesoscale rainband. The horizontal axis perpendicular to the rainband is labelled *S*. In (a), sites A–H are stations having precipitation records. In (b), heavy bars represent the periods at stations A–E during which precipitation fell from a rainband. See text for details.

at that position. If the aircraft was positioned within the rainband, τ was taken to be the average duration of the rainband across the network multiplied by the fraction of the way the aircraft had flown through the rainband. If the aircraft was positioned behind the rainband, τ was taken to be the average duration of the rainband plus the time elapsed since the back edge of the rainband had passed that position.

Step 6: Construction of vertical cross-sections. The τ coordinates were used together with the aircraft's vertical coordinate (pressure, p) to locate the flight path in a vertical (τ–p) cross-section. Events related to the passage of the rainband such as significant changes in surface pressure, temperature, humidity or wind recorded at stations at or near the aircraft's path were also located in the *S*-time plot (Fig. 3(b)), as were the trajectories of rawinsondes. Their τ coordinates could thus be determined, and they could be included in the vertical cross-section along with the aircraft data. Finally, the τ coordinate of the cross-section was converted to horizontal distance by using the average speed of the rainband in the *S* direction across the network.

(*c*) *Locations of fronts in the vertical cross-sections*

The broader features of frontal systems were determined from analyses of satellite imagery and from standard upper air and surface synoptic maps. Serial rawinsondes, launched at intervals of 1 to 3 h, and Doppler radar data enabled mesoscale details in the frontal structures to be resolved. Aircraft temperature data and the finely resolved surface wind, temperature, pressure and humidity measurements included in the τ–p cross-sections were used to position the fronts accurately relative to individual mesoscale rainbands and their associated clouds.

Aircraft measurements were used to locate fronts in two ways. Data collected on horizontal flight legs were examined for horizontal gradients of temperature: the fronts have

been drawn at the warm edges of these zones. Where the aircraft ascended or descended, frontal surfaces were identified from sharp changes in lapse rate.

For the most part, transitions between air masses along the aircraft's path occurred quite sharply. In all cases, frontal positions pinpointed from aircraft data agree very well with positions anticipated from synoptic-scale data and from analyses of serial rawinsondes. In addition, cloud microphysical structure and turbulence measured from the aircraft appear to have been closely related to frontal structure, often changing abruptly when a front was crossed. The dynamical processes related to the frontal structures can, therefore, be invoked to help understand the nature of the clouds present, while the dynamical processes implied by the structures and compositions of the clouds can, in turn, indicate the nature of the airflow in the vicinities of the fronts.

4. Warm frontal rainbands

Figure 4 shows a cross-section through the clouds associated with a mesoscale warm frontal rainband (type 1a in Fig. 1). The positions of the warm front and the potentially unstable layer ($\partial\theta_w/\partial z < 0$, where θ_w is wet-bulb potential temperature and z is height) above it are based on rawinsonde data obtained in the vicinity of the rainband. The isotherm pattern constructed from aircraft data is consistent with the presence of the front and shows a strong horizontal temperature gradient in a very stable layer just below the front.

The existence of general cloudiness throughout the region of the cross-section can be attributed to widespread lifting both above the sloping warm front (as in the model of Bjerknes and Solberg 1922) and below the warm front, within the warm frontal zone (as seen in case studies by Kreitzberg and Brown 1970 and Houze *et al.* 1976b and in the model of Gidel 1978). The cloud features associated with the mesoscale warm frontal rainband were embedded within this region of general ascent and widespread cloudiness.

Marshall (1953) and Plank *et al.* (1955) found that significant warm front precipitation occurs when ice particles, nucleated in shallow convective cells (called 'generating cells') located above the warm front, seed the stable cloud layer below. Browning and Harrold (1969), Houze *et al.* (1976b), and Hobbs and Locatelli (1978) have all noted the presence of such seeding in the vicinities of warm frontal rainbands. The dynamical mechanism that might organize lifting or generate potential instability on the mesoscale, and thereby enhance the precipitation in such a way as to produce a mesoscale warm frontal rainband, is still highly speculative. Kreitzberg and Brown, however, found that potentially unstable air above a warm front tends to arrive behind tongues of warm, moist air that branch from the warm front, and that warm frontal rainbands were consistently associated with such 'leaves' in the warm frontal structure.

In the case presented in Fig. 4 the aircraft flew below the warm front, and no direct observations of generating cells were obtained. The various data that were obtained, however, were all consistent with the presence of generating cells above the warm front. The layer of potentially unstable air above the warm front and behind a warm frontal 'leaf', inferred from rawinsonde data, is similar to the observations of Kreitzberg and Brown; lifting of this potentially unstable air was probably responsible for the shallow layer of convection in cloudy regions above the warm front. Crystal replication indicates that stellar-shaped crystals, which form at temperatures from $-12°$ to $-16°$C, were present in the stratiform cloud above the surface band of rain. Since these temperatures correspond to those in the potentially unstable layer above the warm front, we deduce that ice crystals were introduced into the stratiform cloud from this region, probably by generating cells, which formed as the potential instability was released.

The introduction of ice into the stratiform cloud was apparently an important mecha-

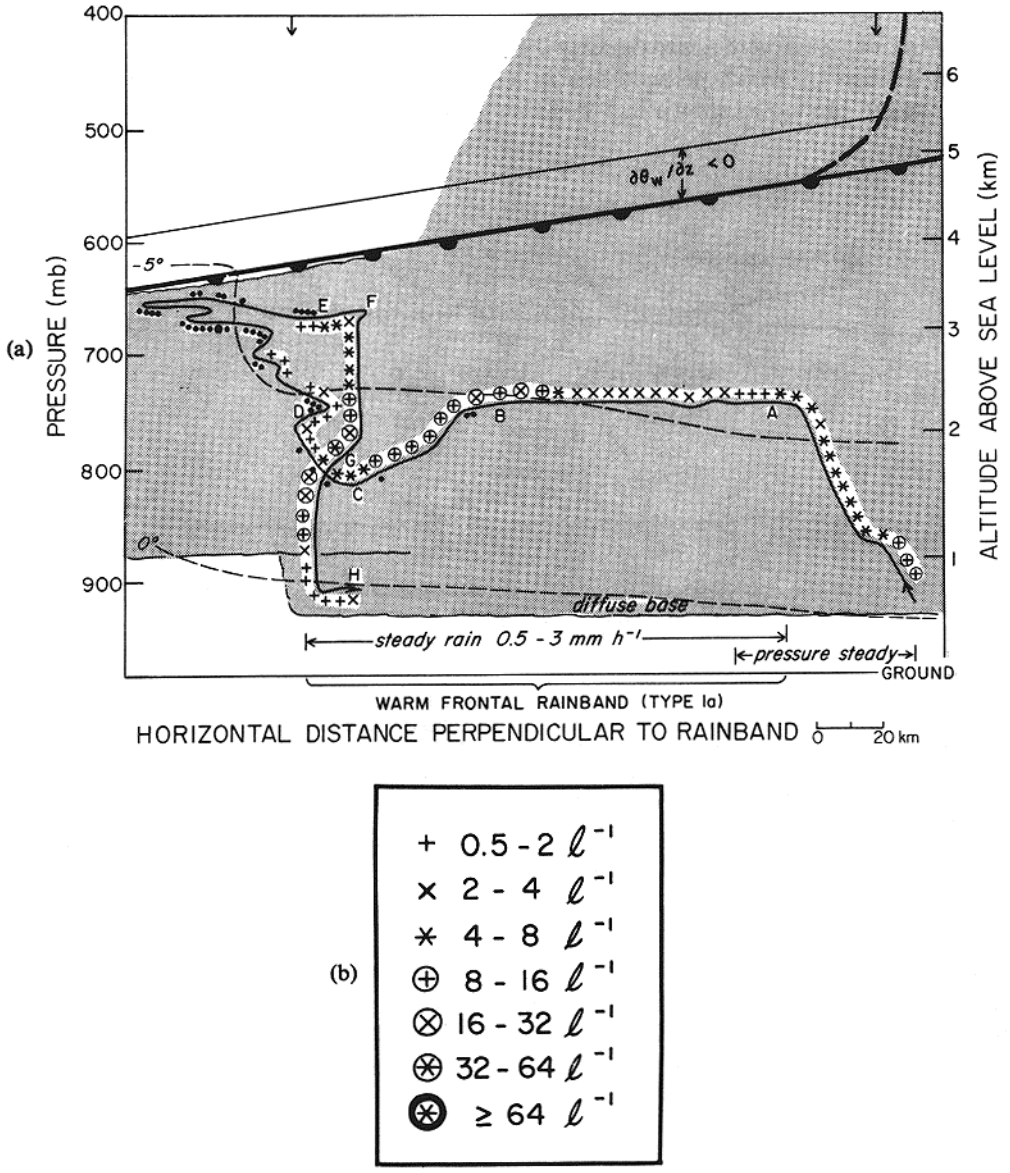

Figure 4. (a) Vertical cross-section through a mesoscale warm frontal rainband (type 1a) on 7 January 1975. The motion of the rainband in the figure is from left to right. The path of the B-23 aircraft is shown by the continuous arrowed line. Smaller and larger dots along the flight path denote cloud liquid water contents from 0·10 to 0·20 and from 0·25 to 0·50 g m^{-3}, respectively. Symbols for ice particle concentrations are explained in Fig. 4(b). Isotherms (thin broken lines) are labelled in °C. The heavy broken line branching out from the front is a warm frontal leaf (see text for explanation). θ_w is wet-bulb potential temperature. Regions of cloud are shaded. Where clouds are outlined, the edges were directly measured or observed; where no outline is drawn, the edge was positioned to be consistent with rawinsondes and other data. Small arrows at the top of the figure indicate positions of rawinsondes. Letters are referred to in the text. (b) Key to symbols used in Figs. 4(a), 6, 10, 11, 12, 14, 15, 16 and 17 to indicate concentrations of ice particles.

nism in the formation of precipitation in the warm frontal rainband, because the regions of the stratiform cloud where ice was nearly or totally absent, and where cloud liquid water contents were as high as 0·25 g m^{-3}, occurred to the rear of the region of mesoscale precipitation at the ground (from D to E in Fig. 4). However, above the region of mesoscale rainfall

(A–D and E–H), the stratiform cloud was glaciated, except for a few small patches where liquid water contents were approximately 0·10 g m^{-3}.

The process by which precipitation in a mesoscale warm frontal rainband grows is summarized in the model shown in Fig. 5. Ice particles nucleated in generating cells aloft

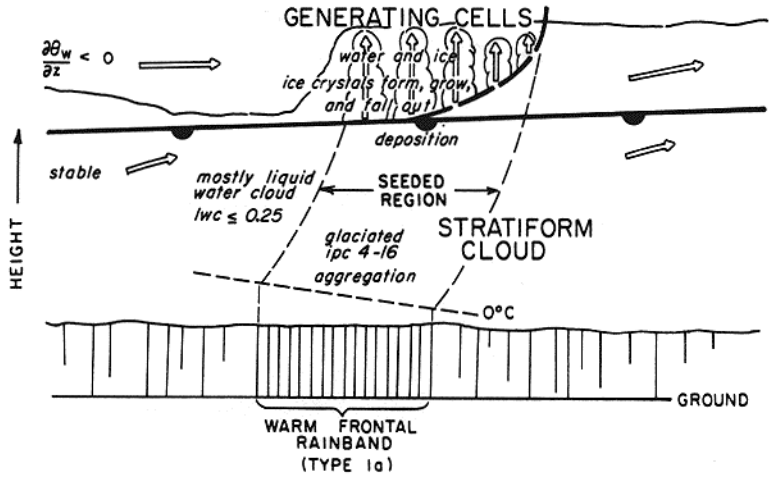

Figure 5. Model of a mesoscale warm frontal rainband (type 1a) shown in vertical cross-section. The structure of the clouds and the predominant mechanisms for precipitation growth are indicated. Vertical hatching below cloud bases represents precipitation; the density of the hatching corresponds qualitatively to the precipitation rate. The heavy, broken line branching out from the front is a warm frontal leaf (see text for explanation). Open arrows depict airflow relative to the warm front and contrast the stable lifting within and above the warm frontal zone with convective ascent in the generating cells. Ice particle concentrations (ipc) are given in numbers per litre; cloud liquid water contents (lwc) are in g m^{-3}. The motion of the rainband in the figure is from left to right.

grow to precipitable size and fall into the stratiform cloud below, growing first by deposition (as shown in Fig. 11 of Houze *et al.* 1976b) and, as they approach the 0°C level, by aggregation. In the case shown in Fig. 4, aggregates were observed throughout the glaciated regions, and the aggregates were seen to increase in size on the descents from B to C and F to G.

5. Warm sector rainbands

Warm sector rainbands (type 2 in Fig. 1) occur within the warm sector of an extratropical cyclone and are oriented parallel to the approaching cold front. The well-known severe midlatitude squall line (Newton 1963) is the most vigorous form of this type of mesoscale rainband. Warm sector rainbands, however, also occur frequently in less energetic forms (Nozumi and Arakawa 1968). In this section, observations of two examples of this weaker type of warm sector rainband are examined (Fig. 6).

The leading warm sector rainband in Fig. 6 appears to have been more convectively active and younger than the second rainband. This is indicated by the presence of cloud liquid water all along the aircraft's path from A to C as well as by the cumuliform appearance of the clouds in this region. The youngest cloud was located between A and B, where the cumuliform elements appeared visually to be new, and where there was a near absence of ice. From B to C, ice particles were observed, but they were found in low concentrations (0·5–2 l^{-1}), and liquid water still dominated the sampled hydrometeors, suggesting that

the trailing portion of the leading warm sector rainband was in an intermediate stage of development. Ice particles in this region were rimed.

In contrast to the leading warm sector rainband, the second rainband in Fig. 6 exhibited little or no cumuliform structure in its visual appearance, and it was almost glaciated between D and E, with only occasional patches of cloud liquid water. It appears, therefore, to have been in a later stage of development than the leading rainband.

The concentrations of ice particles in the second rainband ranged from 5 to 16 l^{-1} along the flight path from D to E, and aggregates of ice particles up to 4 mm in size were much in evidence. The greater age of the second rainband would have allowed time for ice particle concentrations to be increased by fragmentation or some other process, and for

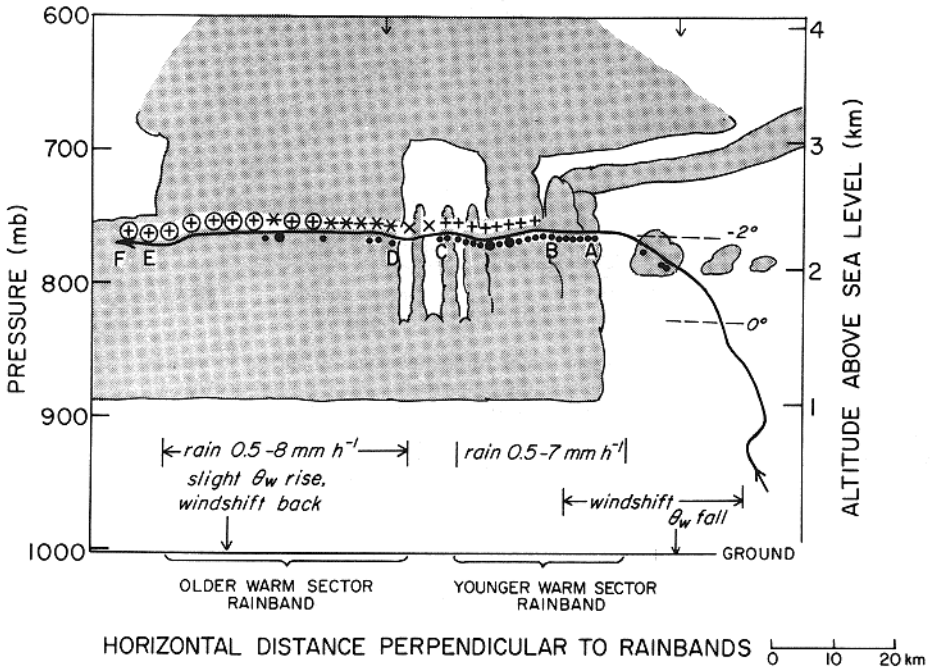

Figure 6. Vertical cross-section through two mesoscale warm sector rainbands (type 2) on 16 December 1974. The path of the B-23 aircraft is shown by the continuous heavy arrowed line. Smaller and larger dots denote cloud liquid water contents from 0·10 to 0·20 and from 0·25 to 0·50 g m^{-3}, respectively. Other symbols and conventions are as in Fig. 4.

the aggregation process to become effective in producing large ice particles. Although the ice particle concentrations remained high just to the rear of the rainband (between E and F), aggregates were not present there, and the individual crystals showed little or no evidence of riming. This observation suggests that collectional growth was crucial in producing the precipitation that fell in the rainband.

Figure 7 summarizes schematically the structure of the two warm sector rainbands. The sequence of a younger, more convectively active rainband followed by an older rainband less convective in appearance suggests a dynamical similarity between these weaker warm sector rainbands and more intense squall-line systems. In both mid-latitude squall lines (Newton 1963) and tropical squall lines (Houze 1977), new active updraughts on the leading edge are followed by older cloud features. Similarity to squall-line dynamics is further indicated by the visual appearance of the approaching clouds, which resembled the

ominous bank of clouds accompanying stronger squall lines. Also, as the precipitation of the warm sector rainbands arrived, a surface windshift occurred, and the wet-bulb potential temperature at ground level decreased markedly, indicating that a precipitation-induced downdraught may have been present, as in more intense squall lines. A sounding taken ahead of the warm sector rainbands showed that the wet-bulb potential temperature in the environment of the rainbands decreased 2°C from the surface to 780 mb; this stratification is consistent with the observed convective structure of the rainbands. A sounding taken through the older rainband was nearly moist-adiabatic and saturated.

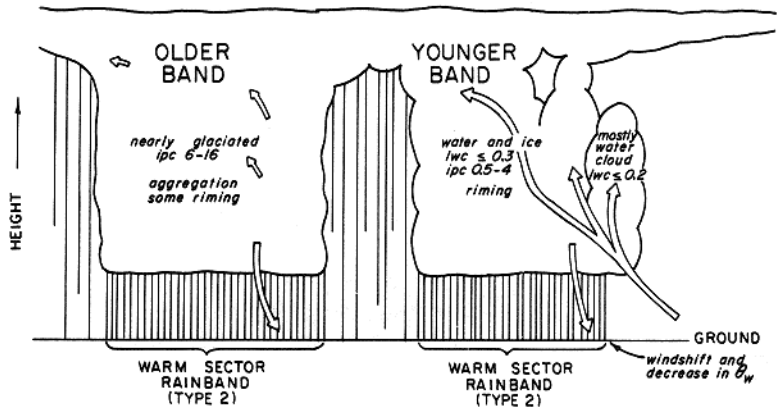

Figure 7. Model of two mesoscale warm sector rainbands (type 2) shown in vertical cross-section. The structure of the clouds and the predominant mechanisms for precipitation growth are indicated. Vertical hatching below cloud bases represents precipitation; the density of the hatching corresponds qualitatively to the precipitation rate. Open arrows depict airflow relative to the rainbands. θ_w is wet-bulb potential temperature. Ice particle concentrations (ipc) are given in numbers per litre; cloud liquid water contents (lwc) are in $g\,m^{-3}$. The motion of the rainbands in the figure is from left to right.

6. Cold frontal rainbands

(*a*) *Model*

The cold front in an extratropical cyclone may extend to the ground, or it may, in a warm-type occlusion, exist only aloft, above the warm frontal surface. In either case, two types of mesoscale rainbands can occur. The narrow cold frontal rainband (type 3a in Fig. 1) occurs with the surface pressure trough at the leading edge of the cold air mass (that is, with the cold front passage at the surface, when the cold front reaches the ground, or with the cold front passage aloft, in a warm-type occlusion). The wide cold frontal rainband (type 3b) may occur in a variety of positions relative to the cold front, ranging from shortly ahead of the surface pressure trough and the leading edge of the cold air mass to a considerable distance to the rear of this position. More than one wide cold frontal rainband may be present, and the narrow cold frontal rainband is often embedded in one of the wide cold frontal rainbands. This mesoscale structure is depicted in a model cross-section in Fig. 8. The components of the model are drawn from four cases discussed in the following sections as well as from several other cases studied during the project. The cumulonimbus towers shown in the model are associated with the narrow cold frontal rainband and may, as depicted, penetrate the widespread frontal cloud shield; perhaps more typically, however, this convection may be sufficiently shallow to be embedded wholly within the widespread clouds (Browning and Harrold 1970; Browning and Pardoe 1973).

ominous bank of clouds accompanying stronger squall lines. Also, as the precipitation of the warm sector rainbands arrived, a surface windshift occurred, and the wet-bulb potential temperature at ground level decreased markedly, indicating that a precipitation-induced downdraught may have been present, as in more intense squall lines. A sounding taken ahead of the warm sector rainbands showed that the wet-bulb potential temperature in the environment of the rainbands decreased 2°C from the surface to 780 mb; this stratification is consistent with the observed convective structure of the rainbands. A sounding taken through the older rainband was nearly moist-adiabatic and saturated.

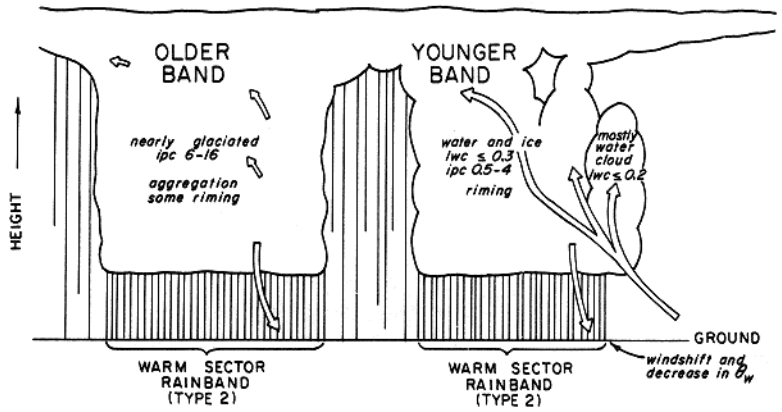

Figure 7. Model of two mesoscale warm sector rainbands (type 2) shown in vertical cross-section. The structure of the clouds and the predominant mechanisms for precipitation growth are indicated. Vertical hatching below cloud bases represents precipitation; the density of the hatching corresponds qualitatively to the precipitation rate. Open arrows depict airflow relative to the rainbands. θ_w is wet-bulb potential temperature. Ice particle concentrations (ipc) are given in numbers per litre; cloud liquid water contents (lwc) are in $g\,m^{-3}$. The motion of the rainbands in the figure is from left to right.

6. Cold frontal rainbands

(*a*) *Model*

The cold front in an extratropical cyclone may extend to the ground, or it may, in a warm-type occlusion, exist only aloft, above the warm frontal surface. In either case, two types of mesoscale rainbands can occur. The narrow cold frontal rainband (type 3a in Fig. 1) occurs with the surface pressure trough at the leading edge of the cold air mass (that is, with the cold front passage at the surface, when the cold front reaches the ground, or with the cold front passage aloft, in a warm-type occlusion). The wide cold frontal rainband (type 3b) may occur in a variety of positions relative to the cold front, ranging from shortly ahead of the surface pressure trough and the leading edge of the cold air mass to a considerable distance to the rear of this position. More than one wide cold frontal rainband may be present, and the narrow cold frontal rainband is often embedded in one of the wide cold frontal rainbands. This mesoscale structure is depicted in a model cross-section in Fig. 8. The components of the model are drawn from four cases discussed in the following sections as well as from several other cases studied during the project. The cumulonimbus towers shown in the model are associated with the narrow cold frontal rainband and may, as depicted, penetrate the widespread frontal cloud shield; perhaps more typically, however, this convection may be sufficiently shallow to be embedded wholly within the widespread clouds (Browning and Harrold 1970; Browning and Pardoe 1973).

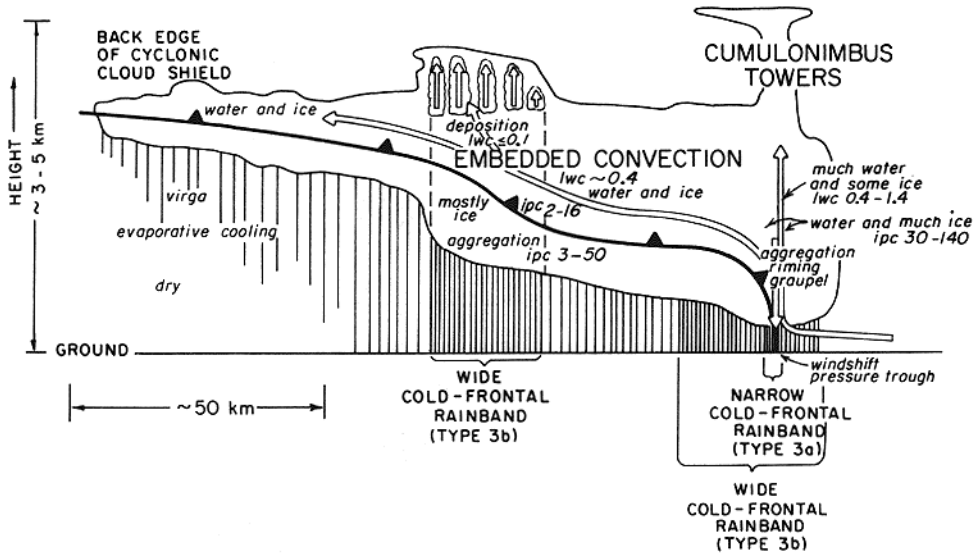

Figure 8. Model of the clouds associated with a cold front showing narrow and wide mesoscale cold frontal rainbands (types 3a and 3b) in vertical cross-section. The structure of the clouds and the predominant mechanisms for precipitation growth are indicated. Vertical hatching below cloud bases represents precipitation; the density of the hatching corresponds qualitatively to the precipitation rate. Open arrows depict airflow relative to the front: a strong convective updraught and downdraught above the surface front and pressure trough, and broader ascent over the cold front aloft. Ice particle concentrations (ipc) are given in numbers per litre; cloud liquid water contents (lwc) are in $g m^{-3}$. The motion of the rainband in the figure is from left to right. Horizontal and vertical scales are approximate, but typical of aircraft and radar observations in specific cases.

(*b*) *Cold frontal air motions*

The model airflow depicted in Fig. 8 is similar to that observed by Browning and Harrold (1970) and is further verified by our Doppler radar measurements. An example is shown in Fig. 9. This airflow pattern was determined by applying the equation of continuity to the horizontal component of the measured velocity in a vertical plane oriented perpendicular to the front. Vertical velocities of the air were calculated by assuming that no significant horizontal divergence occurred in the wind component parallel to the front and by integrating the cross-front divergence upwards in 0·33 km steps from the surface, where a vertical velocity of zero was assumed. Figure 9 was obtained by combining measured horizontal velocities relative to the front with computed vertical velocities.

The resulting relative airflow pattern shows that the narrow cold frontal rainband was associated with a narrow updraught having a maximum vertical velocity of $1 m s^{-1}$. This updraught occurred directly above strong, low-level convergence ($1{\cdot}9 \times 10^{-3} s^{-1}$) at the frontal windshift line, where air in the boundary layer flowed, in a relative sense, towards the cold front. Browning and Harrold (1970) found a peak convergence of about a factor of 4 to 5 higher than ours, corresponding to larger rainfall rates observed in their case. As in the model (Fig. 8), a narrow downdraught occurred adjacent to the updraught (at 20 km in Fig. 9) but did not extend through as deep a layer as the updraught. In this case, however the downdraught occurred ahead of rather than behind the updraught. That the updraughts and downdraughts associated with narrow cold frontal rainbands may occur in highly organized configurations is suggested by the work of Hobbs and Biswas (1979), who have shown that the precipitation in these rainbands is commonly organized into patterns of regularly spaced, small mesoscale elements.

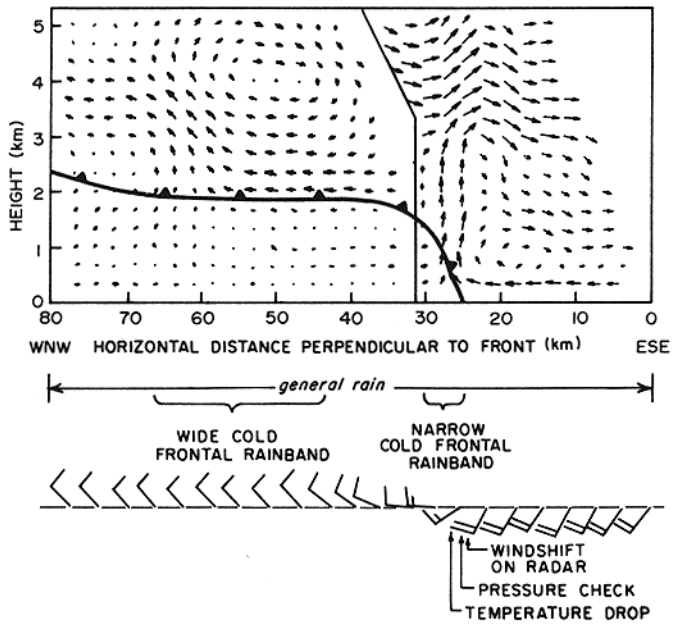

Figure 9. Vertical cross-section showing the airflow relative to a cold front as it was observed with the CP-3 Doppler radar on 17 November 1976. At this time, the radar was located at Pt Brown, Washington (Figure 2). The arrows represent 5 min displacements. The heavy vertical seam separates airflows calculated from two different radar scans, 30 min apart, which have been joined to produce a composite picture. The cold front was located at the top of the layer of cold advection, as determined from vertical wind shear. The position of the windshift at the surface seen with the radar is indicated at the bottom of the figure. Also shown are a wind record and other surface information from the radar site, positioned along the cross-section using the speed of the front to convert time to distance.

In the region of the wide cold frontal rainband in Fig. 9, the general ascent over the front was enhanced. The maximum vertical velocity in this region was 50 cm s^{-1}. Below the cold front, practically no vertical motions existed in the region of the wide cold frontal rainband. This case is discussed in further detail by Hobbs *et al.* (1978).

(*c*) *Cold fronts sampled by aircraft*

The cloud microphysical structure shown in the model in Fig. 8, as well as further details of the air motions associated with narrow and wide cold frontal rainbands, have been verified by direct aircraft sampling of cold frontal clouds. Vertical cross-sections containing aircraft data for three different types of cold front are shown in Figs. 10–12. The case of 16 January 1974 (Fig. 10) was a non-occluded cold front. Synoptic maps and satellite pictures indicate that the other two cases, 2 and 7 January 1975, were occluded frontal systems. On 2 January 1975 (Fig. 11), upper air data confirm that a warm frontal structure, with strong warm air advection, existed aloft in the leading portion of the system, while surface, aircraft, and rawinsonde data established that this structure was followed by a well-defined cold front that extended down to the ground. Hence, this case resembled a classical cold occlusion; however, for reasons discussed below, it was unlikely that the warm front intersected the cold front as in the classical case. On 7 January 1975 (Fig. 12), serial rawinsondes and aircraft data show that a cold front was advancing over a warm front, as in a classical warm-type occlusion. A brief rise in surface pressure, occurring within a general falling trend, was recorded as the upper-level cold front passed, but no surface frontal passage occurred during the period shown in the cross-section.

Despite the different synoptic situations represented by these three cases, the cold fronts had remarkably similar structures of mesoscale rainbands. These similarities are most evident in the aircraft data, discussed below. In addition to the three cases described here, we have examined aircraft data in four other cold frontal cases, and basic similarities were found in all the cases.

(*d*) *Narrow cold frontal rainbands*

In each of the three cases shown in Figs. 10–12, a narrow cold frontal rainband (type

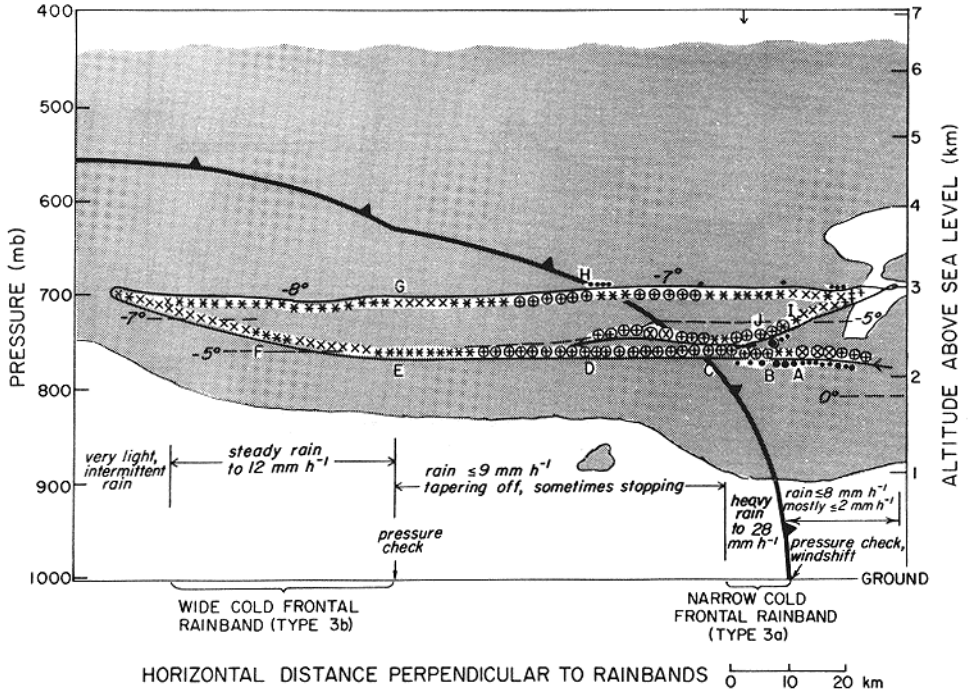

Figure 10. Vertical cross-section through mesoscale cold frontal rainbands (types 3a and 3b) on 16 December 1974. The path of the B-23 aircraft is shown by the continuous arrowed line. Small, medium, large, and circumscribed large dots on the flight path denote cloud liquid water contents from 0·10 to 0·20, 0·25 to 0·50, 0·55 to 0·95, and $\geqslant 1{\cdot}00\,\mathrm{g\,m^{-3}}$, respectively. Other symbols and conventions are as in Figure 4.

3a) occurred, and the B-23 aircraft passed through the narrow updraught region corresponding to the rainband. The position of the narrow updraught in each case is consistent with the model in Fig. 8.

On 16 December 1974 the updraught (A–B and I–J in Fig. 10) was not measured directly, but it can be inferred from the cloud microphysical observations. In the two other cases, the updraughts were not only evident in the microphysical data, but were indicated by the vertical displacements of the aircraft, visible in the cross-sections. On 2 January 1975 the narrow updraught was $2–3\,\mathrm{m\,s^{-1}}$ in magnitude and 4 km in width at low levels (A–B in Fig. 11). Immediately behind the updraught (B–C), a downdraught of similar magnitude and width occurred in a pattern consistent with the model in Fig. 8. In the cloud tower at upper levels (F–I) the updraught was again encountered (between G and H) and was a few metres per second in magnitude. A similar, narrow updraught–downdraught pair was observed on 7 January 1975 (B–D in Fig. 12). In this case the updraught and downdraught were each $2–3\,\mathrm{m\,s^{-1}}$ in magnitude and 0·7 km in width.

On 16 December 1974 and 2 January 1975 sharp surface frontal passages occurred. The narrow updraughts encountered by the aircraft in these two cases were apparently associated with strong convergence in the boundary layer towards the frontal pressure troughs and windshift lines. With such a strong updraught extending upwards from the boundary layer, it does not seem possible that the warm front in Fig. 11 could have intersected the cold front. On 7 January 1975 the cold front did not extend to the ground, and the narrow updraught in this case was located aloft without any apparent connection to strong convergence at low levels.

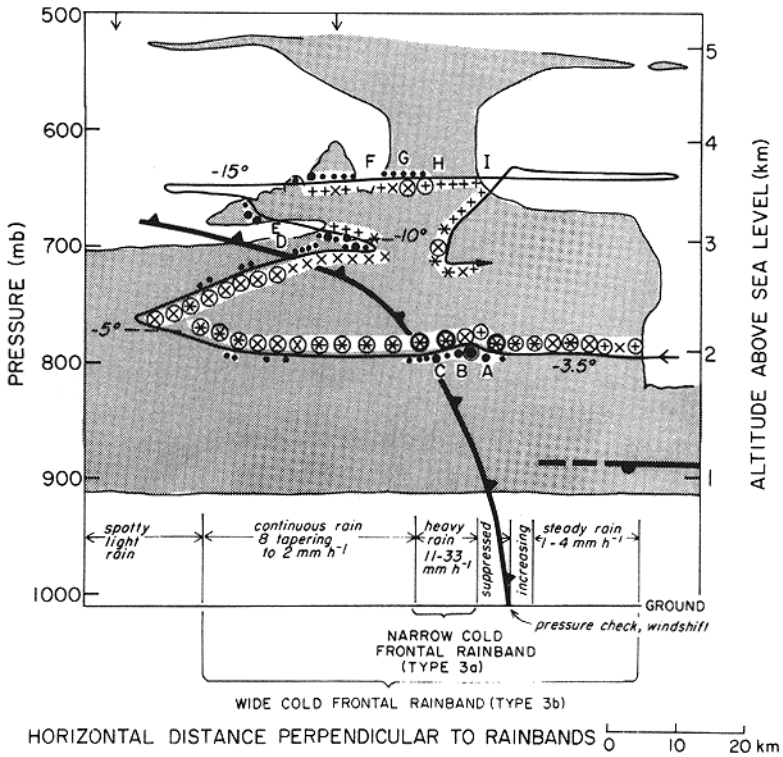

Figure 11. Vertical cross-section through mesoscale cold frontal rainbands (types 3a and 3b) on 2 January 1975. The path of the B-23 aircraft is shown by the continuous arrowed line. Small, medium, and circumscribed large dots on the flight path denote cloud liquid water contents from 0·10 to 0·20, 0·25 to 0·50, and $\geqslant 1{\cdot}00\,g\,m^{-3}$, respectively. Other symbols and conventions are as in Fig. 4.

The microphysical structure of the cloud in each of the narrow updraughts was that of a young, vigorous convective cloud element. Liquid water contents, with maximum values of 0·45 to $1{\cdot}40\,g\,m^{-3}$, were found near each of the updraught cores. These peak values of observed cloud liquid water content ranged from 50 to 100% of computed adiabatic values. Ice particles in the updraughts showed heavy riming: rimed aggregates and graupel up to several millimetres in diameter were observed on 16 December, between A and B in Fig. 10, on 2 January, between A and B in Fig. 11, and on 7 January, between B and C in Fig. 12. Similar evidence of riming was not found on the upper-level pass between G and H on 2 January. This observation indicates that riming was important as a precipitation growth mechanism only in the lower portion of the narrow updraught.

The youth of the cloud elements in the narrow updraughts is indicated not only by their relatively high cloud liquid water contents, but also by the ice particle concentrations in the updraught cores, which were one half to one tenth the concentrations in the surround-

ing clouds. The adjacent narrow downdraughts, in particular, had much higher ice particle concentrations than did the updraughts. On 7 January the youth of the cloud elements in the updraught relative to the surrounding cloud was further indicated by the sampling of large ice needles, up to 0·7 mm in length, from A to B in Fig. 12, just ahead of the updraught, and from C–D, just behind the updraught, whereas, in the updraught itself (B–C) ice needles had attained a maximum length of only 0·1 mm, suggesting much more recent nucleation.

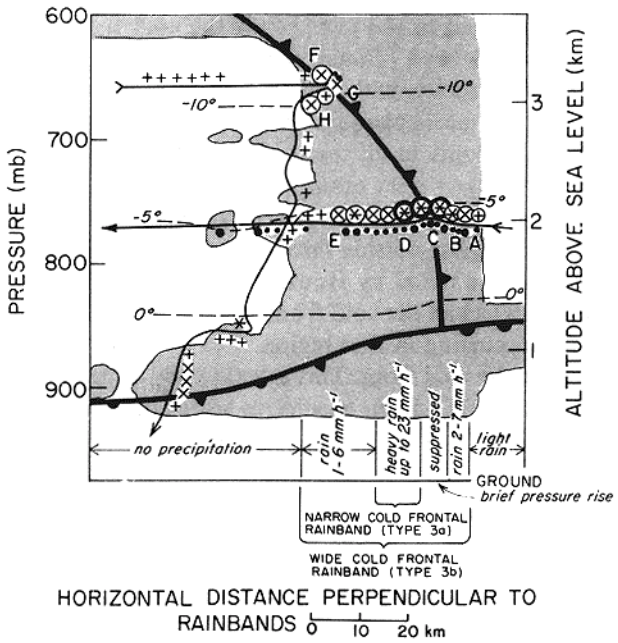

Figure 12. Vertical cross-section through mesoscale cold frontal rainbands (types 3a and 3b) on 7 January 1975. The path of the B-23 aircraft is shown by the continuous arrowed line. Smaller and larger dots on the flight path denote cloud liquid water contents from 0·10 to 0·20 and from 0·25 to 0·50 g m^{-3}, respectively. Other symbols and conventions are as in Fig. 4.

Growing precipitation particles in the narrow updraughts were evidently suspended aloft, as the short burst of heavy rain constituting the narrow cold frontal rainband at the surface lagged the updraught by a few kilometres in all three cases, while the rainfall directly under the updraught was, in two of the cases, markedly suppressed (Figs. 11 and 12). This was particularly well documented in the case of 2 January. The aircraft was flying directly over the high resolution raingauge at Aberdeen (Fig. 2) when the narrow updraught–downdraught pair was encountered. The precipitation rate, which had increased for a few minutes immediately ahead of the front, was suppressed for 5 min. After the passage of the updraught overhead, the heavy burst of rain occurred with precipitation rates over 30 mm h^{-1}. The sequence of a brief increase in rainfall rate, followed by a suppressed rainfall rate and then a short burst of heavy precipitation, was also observed at other stations over which the cold front passed. Browning and Harrold (1970) also noted a suppression of the radar echo intensity (i.e. rainfall rate) in the narrow updraught core. The suppression of precipitation in the updraught, with the heavy rain coinciding more closely with the downdraught, is rather typical of convective updraughts. Hydrometeors in the updraught are recently formed, tending to be small. Larger particles with appreciable terminal velocities provide negative buoyancy for downdraughts. Browning and Harrold compare the suppression of rainfall in the narrow updraught with the weak echo vault observed in severe convective storms.

(e) *Wide cold frontal rainbands*

A wide cold frontal rainband (type 3b) occurred on 16 December (Fig. 10) 70 km to the rear of the narrow cold frontal rainband. The narrow and the wide cold frontal rainbands on this day were embedded within a broader region of frontal cloud and light precipitation. On both 2 and 7 January (Figs. 11 and 12), the precipitation pattern consisted of a single wide cold frontal rainband within which the narrow cold frontal rainband was embedded.

When aircraft measurements made within the horizontal boundaries of the wide cold frontal rainbands were obtained at altitudes below the cold front (E–G on 16 December, C–D on 2 January, D–E and G–H on 7 January), the clouds were found everywhere to contain large concentrations of ice particles, with amounts of cloud liquid water varying from case to case. The primary growth mechanism for the ice particles was aggregation. Aggregates were noted below the cold fronts in all three cases in Figs. 10–12. The cold front on 16 December provided a particularly clear example of the importance of aggregation in a wide cold frontal rainband; aggregates replicated at F in the wide rainband were more numerous and tended to be larger than those outside the rainband. Evidence for aggregation in a wide cold frontal rainband was also noted by Houze *et al.* (1976b).

Aircraft measurements below the cold front on 16 December (C–H in Fig. 10) give no indication of any lifting occurring in that region. The ice particles observed had therefore originated in ascent above the cold front. This is verified by a sudden change in crystal type, encountered by the aircraft at D, from needles to plates (which nucleate at temperatures from -3 to -8°C and from -8 to -12°C, respectively), a change coincident with the elevation of the region of lifting above the front to levels colder than -8°C.

Aircraft measurements in the wide cold frontal rainband on 2 January that were obtained above the cold front (D–F in Fig. 11) show that cloud liquid water was more prevalent, and that turbulence was stronger and more prevalent, above the cold front than below it. Small convective towers were also observed between E and F. These observations are consistent with the model in Fig. 8, which shows that the region of enhanced lifting producing wide cold frontal rainbands occurs above the front and contains embedded convective cloud elements. Radar echo patterns aloft in wide cold frontal rainbands typically show such cumulus-scale irregularities (e.g. Fig. 8 of Browning and Harrold 1970; Fig. 12 of Houze *et al.* 1976b).

The microphysical pattern was somewhat more complicated on 7 January. Cloud liquid water and turbulence were measured not only above the cold front (F–G in Fig. 12), but also immediately behind the cold front from D to E. This case, therefore, shows that the ascent associated with wide cold frontal rainbands may sometimes occur both above the cold front and within the cold frontal zone itself. In this case the generation of potential instability by the advance of the cold air mass aloft may have been important in causing the vigorous ascent between D and E.

7. Prefrontal surges

(a) *Model*

In mesoscale analyses of occluded frontal systems, Kreitzberg (1964), Kreitzberg and Brown (1970) and Browning *et al.* (1973) found that the frontal zone leading the cold air mass sometimes contains several hyperbaroclinic zones which give the cold air mass the appearance of arriving in a series of pulses. In an ordinary synoptic analysis the strongest pulse would probably be identified as the cold front. The weaker pulses usually occur ahead of the strongest pulse, above the warm front, and their thermal structures become apparent only when mesoscale rawinsonde or aircraft coverage is available. These weak frontal pulses,

called 'prefrontal surges', have an important effect on the mesoscale pattern of the precipitation ahead of the cold front in an occlusion.

Two types of mesoscale rainband may be associated with the passage aloft of a prefrontal cold surge; these are illustrated in the model cross-section in Fig. 13. The first type of rainband, shown on the right in Fig. 13, is a deep and wide mesoscale band of cloud and

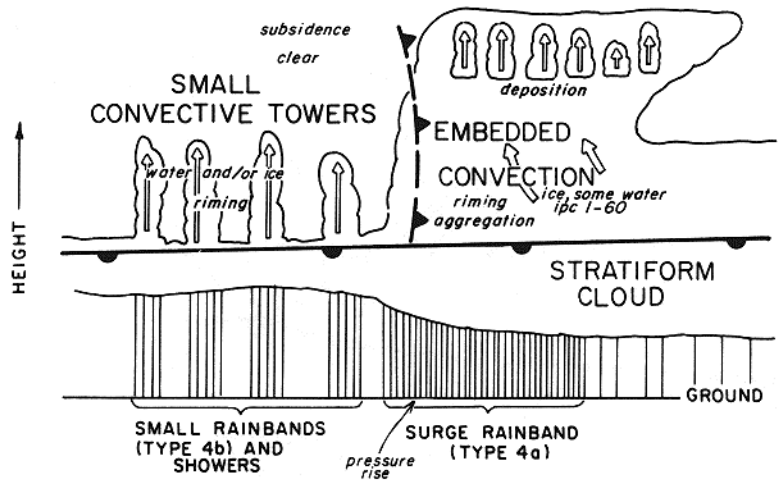

Figure 13. Model of mesoscale rainbands (types 4a and 4b) associated with a prefrontal surge of cold air aloft, ahead of an occluded front. The broken cold front symbol indicates the leading edge of the surge. (The primary cold front is off the figure to the left.) The structure of the clouds and the predominant mechanisms for precipitation growth are indicated. Vertical hatching below cloud bases represents precipitation; the density of the hatching corresponds qualitatively to the precipitation rate. Open arrows depict airflow relative to the cold surge and convective ascent. Ice particle concentrations (ipc) are given in numbers per litre. The motion of the cold surge and the rainbands in the figure is from left to right.

precipitation that precedes or straddles the leading edge of the prefrontal surge, whose passage overhead is marked at the surface by a temporary, slight rise in pressure (or a lessening in its general fall). This rainband, here called the 'surge rainband' (type 4a in Fig. 1), is similar to a wide cold frontal rainband, although it often appears less coherent on radar than rainbands associated with the primary cold front. Radar data indicate that it contains embedded convection.

Behind the surge rainband, within the mesoscale region of cold air, is a zone of subsidence, which suppresses upper cloud layers (Kreitzberg and Brown 1970). However, a field of convection may develop in this region just above the warm front as potential instability, generated by the cold air of the prefrontal surge overrunning the warm front, is released. This convection, which penetrates into the air of the prefrontal cold surge aloft (left half of Fig. 13), can be spotty, but it sometimes occurs in sharply defined, small mesoscale rainbands (type 4b in Fig. 1). Three examples of the cloud structures associated with prefrontal surges are shown in Figs. 14–16.

(*b*) *2 January 1975*

The vertical cross-section for this case (Fig. 14) contains most of the features shown in the model. Precipitation associated with the surge rainband (type 4a) fell as rain, up to $4\,\mathrm{mm\,h^{-1}}$ in intensity, at coastal stations, but occurred only as virga inland, as the air in

lower layers was dry. A distinct rise in pressure, associated with the passage aloft of the leading edge of the cold surge, was tracked across the data network with the surge rainband. The precipitation that fell from the field of convection behind the surge rainband was spotty in this case.

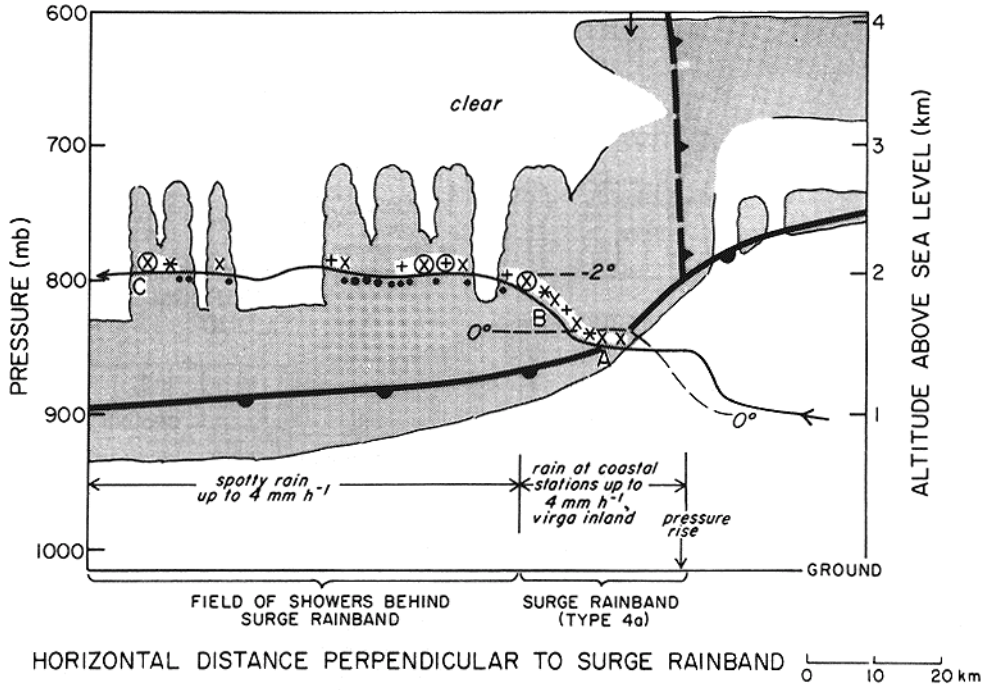

Figure 14. Vertical cross-section through a surge rainband (type 4a) and the field of convection following it on 2 January 1975. The leading edge of the prefrontal cold surge is indicated by a broken cold front symbol. The path of the B-23 aircraft is shown by the continuous arrowed line. Smaller and larger dots on the flight path denote cloud liquid water contents from 0·10 to 0·20 and from 0·25 to 0·50 g m^{-3}, respectively. Other symbols and conventions are as in Fig. 4.

Aircraft measurements from A to B in Fig. 14 were obtained in the cloud associated with the surge rainband. No cloud liquid water was observed, and ice particles were present in concentrations of 1 to 6 l^{-1}. In this respect, the surge rainband resembled warm frontal rainbands (type 1a), older warm sector rainbands (type 2), and wide cold frontal rainbands (type 3b), all of which usually contain rather homogeneous and nearly glaciated regions where ice particle concentrations range from 1 to 60 l^{-1}. As in these other rainbands, aggregation appears to have been an important mechanism in the surge rainband for growth of the ice particles, as both small (1 mm) and a few large (up to 4 mm) aggregates were observed between A and B.

The clouds changed to a more convective type at B in Fig. 14, becoming less homogeneous and more turbulent. From B to C the aircraft passed through isolated convective towers and clusters of towers in various stages of maturity. Some of the towers, evidently the younger ones, contained supercooled cloud water (in amounts up to 0·40 g m^{-3}) and little or no ice, while apparently older towers had high ice particle concentrations (up to 30 l^{-1}) and little or no liquid water. The ice particles included needles, assemblages of needles, and aggregates up to 2 mm in diameter, consistent with the rather high temperatures in the clouds.

(c) *7 January 1975*

The prefrontal surge in this case was a strong feature, marked at its leading edge by a zone of large horizontal gradient of wet-bulb potential temperature above the warm front. A surge rainband (type 4a) accompanied the leading edge of the cold surge, and this was followed immediately by a field of convection arranged in sharply defined lines (type 4b rainbands). These lines were strongly cellular in appearance on radar and were aligned nearly perpendicular to the wind at their level. This orientation, which is not parallel to the cold front or the surge rainband, is typical of this situation and is depicted in Fig. 1.

The B-23 aircraft flew through a portion of these lines of convection, and the measurements obtained are shown in Fig. 15. Convective towers were observed to be rising from a lower-level stratiform cloud deck, sometimes broken, along the warm front. No upper-level cloud was present. The convective towers all showed evidence of active updraughts. Quite large cloud liquid water contents were present nearly everywhere in the towers. At A and D, the aircraft experienced strong upward air motions ($\sim 2\,m\,s^{-1}$ at D), and its vertical displacements are apparent in the figure. As in the case of 2 January, the towers behind the surge rainband appear to have been in various stages of development. Towers A and B contained mostly cloud liquid water and very little ice, indicating that they were quite young. Tower C contained a mixture of liquid and ice. Tower D was especially vigorous, with clearly differentiated regions of ascent, marked by liquid water contents reaching $1{\cdot}25\,g\,m^{-3}$ and little ice, and descent, in which cloud liquid water contents were low and ice particle concentrations reached $64\ l^{-1}$.

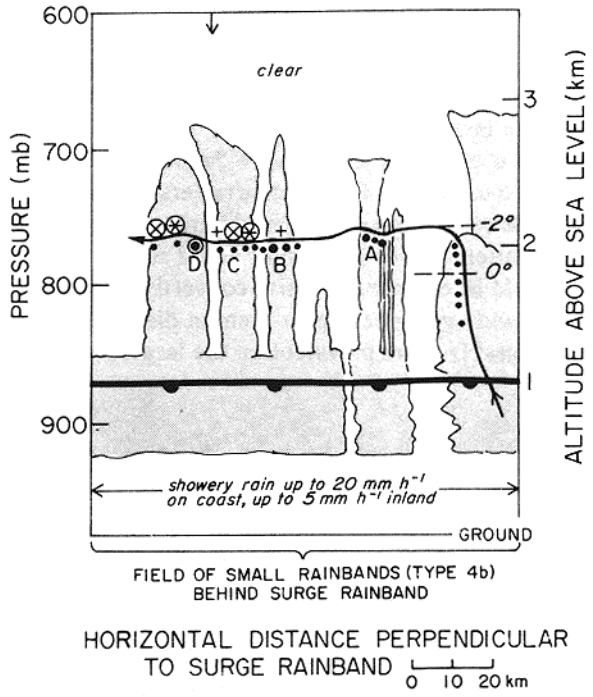

Figure 15. Vertical cross-section through mesoscale rainbands, type 4b, on 7 January 1975, which followed the leading edge of a prefrontal cold surge aloft and a surge rainband (type 4a), off the figure to the right. The path of the B-23 aircraft is shown by the continuous arrowed line. Small, medium, large, and large circumscribed dots on the flight path denote cloud liquid water contents from 0·10 to 0·20, 0·25 to 0·50, 0·55 to 0·95, and $\geqslant 1{\cdot}00\,g\,m^{-3}$, respectively. Other symbols and conventions are as in Fig. 4.

(*d*) *10 January 1976*

The passage of the leading edge of the prefrontal surge in this case was marked by a slight rise in surface pressure. Both the B-23 and the Sabreliner aircraft recorded temperature falls as they crossed the front of the surge. A shift in wind through a deep layer, observed with the CP-3 Doppler radar, occurred as the leading edge of the surge passed. The precipitation associated with the prefrontal surge had just begun its development into a coherent surge rainband as it moved across the data network. Figure 16(a) shows microphysical data collected with the B-23 aircraft and the cloud structure encountered along its flight path. A cross-section of radar reflectivity data along the flight path, almost coincident in time with the flight, is also shown. Figure 16(b) shows data from the Sabreliner aircraft in the same cloud features.

The clouds associated with the surge rainband straddling the leading edge of the prefrontal surge were penetrated by the B-23 aircraft between B and D and by the Sabreliner between AA and BB and between CC and DD. The feature located between A and B in Fig. 16(a) could be seen on radar to be a small, isolated protuberance extending from the leading edge of the surge rainband, and is not considered part of the rainband proper.

The surge rainband contained ice particles in concentrations of 7 to 60 l^{-1}. The ice particles included needles, assemblages of needles, and aggregates as large as 3 to 4 mm in diameter. Thus, aggregation again appears to have been an important mechanism for the growth of ice particles, as in other types of rainband where broad regions of high ice particle concentrations occur. Light to moderate riming was generally observed on the replicated ice particles in this case.

The region from B to C in Fig. 16(a) was nearly glaciated. Between C and D, behind the leading edge of the prefrontal surge, the B-23 aircraft encountered increasing amounts of cloud liquid water. This region was a zone of transition between the surge rainband and the field of convection encountered between D and F. The higher liquid water contents between C and D apparently led to the observation in that region of occasionally heavier riming on ice particles than between B and C.

As in the previous two examples on 2 and 7 January 1975, the field of convection following the surge rainband consisted of convective towers extending upwards from a lower, stratiform cloud layer. The towers were again in different stages of development, as they contained various combinations of ice and cloud liquid water. Riming was variable, but occasionally heavy, as would be expected in active convective towers. Needles were the only recognizable crystal type, and aggregates up to 3 mm in diameter, containing needles, were sampled. Riming was noticeably more prevalent on the larger ice particles than on smaller, individual needles.

8. Postfrontal rainbands

Postfrontal rainbands (type 5 in Fig. 1) occur in the cold air mass well to the rear of the cold frontal zone. These bands can often be observed both visually and in satellite imagery, since they are usually neither obscured by a cirrus shield nor embedded in widespread layer clouds associated with the frontal system. The polar air mass is convectively unstable in its lower layers, and the postfrontal rainbands are convective with strongly showery precipitation. The convection develops in response to the heating and saturation of the surface layer as the air mass moves over the warm ocean surface prior to its landfall. The occasional arrangement of this convection in postfrontal bands indicates the presence of some mesoscale organizing feature. The orientation of postfrontal rainbands parallel to the cold front, time sections of serial rawinsonde data, and the behaviour of surface

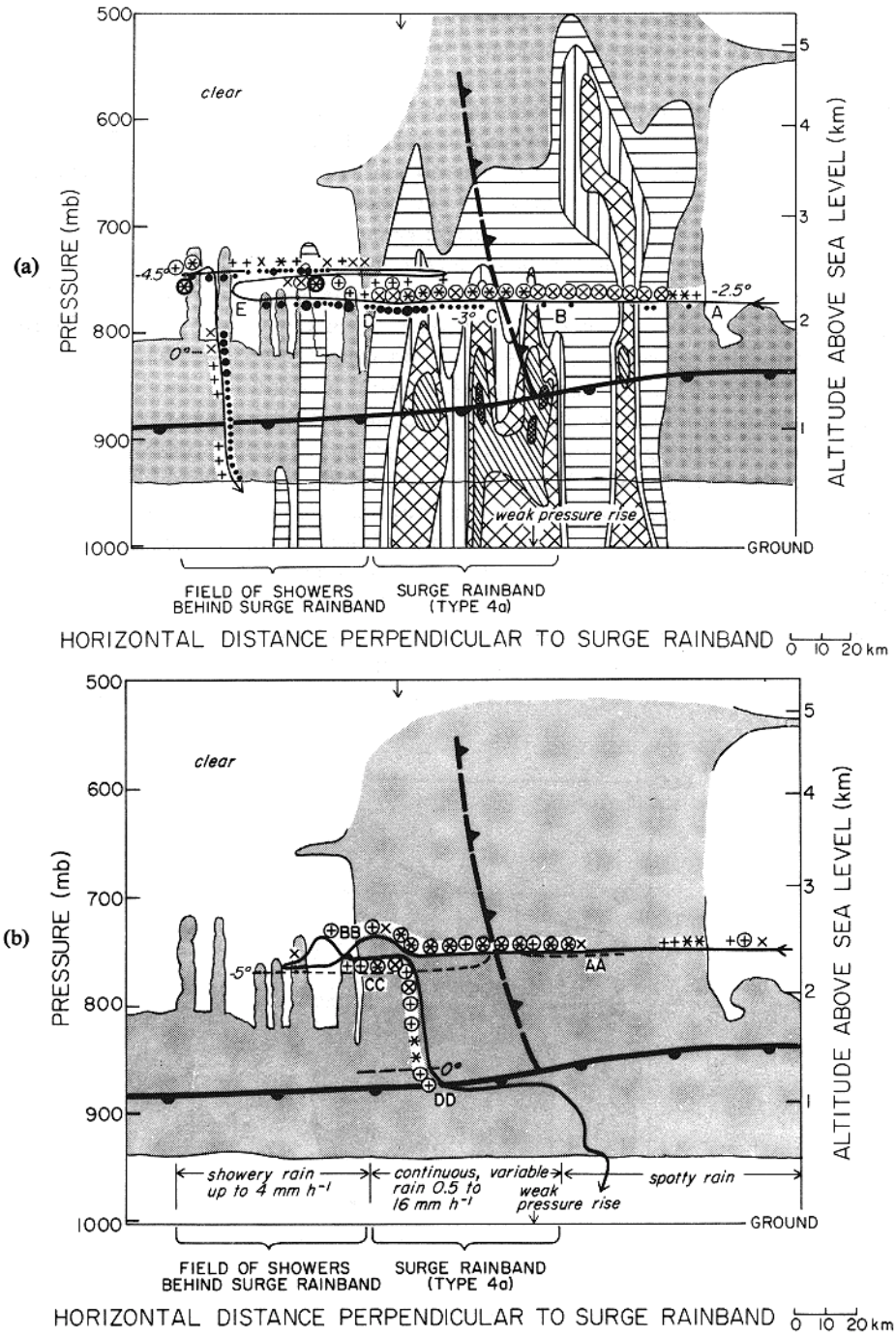

Figure 16. Vertical cross-sections through a mesoscale surge rainband (type 4a) and the field of convective rainbands following it (type 4b) on 10 January 1976. The leading edge of the prefrontal cold surge is indicated by a broken cold front symbol. In (a), the path of the B-23 aircraft is shown by the continuous arrowed line. Small, medium and large dots on the flight path denote cloud liquid water contents from 0·10 to 0·20, 0·25 to 0·50, and 0·55 to 0·95 g m^{-3}, respectively. Regions of radar reflectivity along the path of the aircraft are shown by hatching for contours of 12, 22, 27, 32, and 37 dBZ. In (b), the path of the Sabreliner aircraft is shown by the continuous, arrowed line. The outlines of the clouds, shown in (a) and determined from observations made on board the B-23, have been duplicated in (b) to serve as a reference. Other symbols and conventions are as in Fig. 4.

pressure, temperature and winds during the passages of postfrontal rainbands suggest that these rainbands may sometimes be associated with secondary frontal zones within the polar air mass, similar to those described by Bjerknes and Solberg (1922).

The degree to which postfrontal rainbands may be related to the dynamics of secondary frontal zones is not yet clear and may vary considerably. Houze *et al.* (1976a) described a postfrontal rainband that was relatively narrow and strongly cellular and in which a new line of cells formed immediately ahead of the existing line of decaying cells, thereby apparently behaving as an organized convective system. The case presented in Fig. 17 also had a convective appearance, but this postfrontal rainband was wider and was accompanied by a deep layer of cooling and a decrease in wet-bulb potential temperature. This horizontal temperature contrast was measured both by serial rawinsondes and by the B-23 aircraft. These measurements, taken ahead of, within, and behind the clouds associated with the postfrontal rainband, show that the measured gradient was not due merely to temperature variations within the convective clouds, and a secondary cold front has been drawn in the cross-section at the leading edge of the zone of cooling. A surface pressure check accompanied the rainband across the data network. Although no significant cirrus cloud was noted overhead during the aircraft flight, an infrared satellite picture taken 3 h after the flight shows that a comma-shaped canopy of high cloud had formed above and to the rear of the postfrontal rainband, and data from radar and raingauges indicate that a series of postfrontal rainbands following the first postfrontal band were located under this canopy.

During the B-23 aircraft's penetration of the postfrontal rainband, lightning was observed at A, verifying the convective nature of the clouds. Since postfrontal rainbands are strongly cellular and showery, the microphysical measurements obtained in these clouds

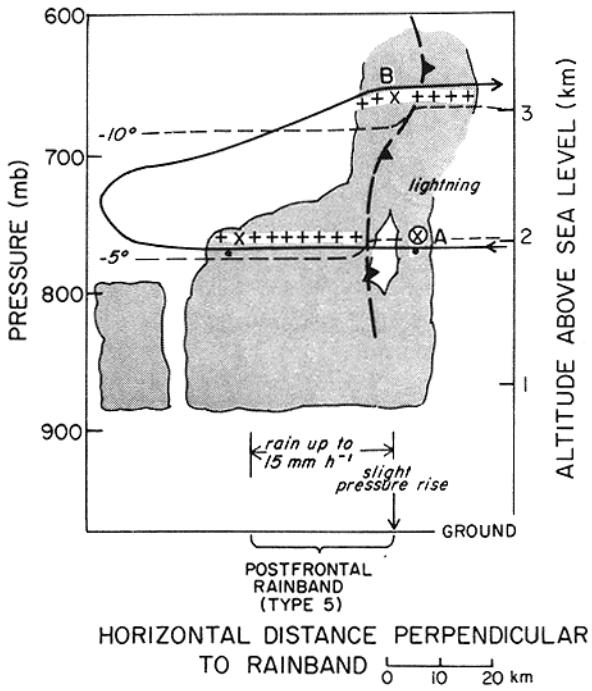

Figure 17. Vertical cross-section through a postfrontal rainband (type 5) on 7 January 1975. The path of the B-23 aircraft is shown by the continuous arrowed line. Dots on the flight path indicate cloud liquid water contents from 0·10 to 0·20 g m^{-3}. The broken cold frontal symbol indicates a secondary cold front within the cold air mass. Other symbols and conventions are as in Fig. 4.

will vary, depending on the ages of the elements penetrated. In the case shown in Fig. 17 the cloud was evidently old, as it was nearly glaciated. At B, light to moderate riming was observed on ice crystals, indicating the earlier presence of supercooled water. Postfrontal rainbands commonly produce heavy showers of graupel; therefore large quantities of supercooled water must typically be present in the earlier stages of these convective features.

9. Conclusions

Aircraft measurements have revealed important aspects of the clouds associated with the major types of mesoscale precipitation features in extratropical cyclones. Each of the types of mesoscale rainband studied was associated with a cloud structure distinctly related to the horizontal and vertical structure of fronts and air masses, and the precipitation association with each type of feature appears to have resulted from distinct dynamical and microphysical processes.

Warm frontal rainbands arise when precipitation becomes enhanced in a mesoscale region embedded within the widespread area of cloudiness associated with warm frontal lifting. Seeding of the stable cloud layer below the warm front with ice particles nucleated in shallow convective cells located above the warm front appears to be a particularly important mechanism in the production of the precipitation. This seeding can nearly glaciate the stable cloud layer, where ice particles then grow by aggregation.

Warm sector rainbands are observed occasionally as intense squall lines and more commonly in a much weaker form. The weak warm sector rainbands appear nevertheless to be dynamically similar to the intense squall lines, with a sequence of younger, more active convective elements, containing large amounts of cloud liquid water, followed by older, glaciated cloud elements. There is evidence that, as in more intense squall lines, a downdraught spreads out below the older elements, giving rise to a gust front, above which unstable air is lifted and new convective elements form.

Two types of cold frontal rainband can occur within the general region of upward motion associated with a cold front. Wide cold frontal rainbands occur when lifting over the cold front is enhanced in a region several tens of kilometres in width. Vertical velocities in this region of enhanced lifting can be several tens of centimetres per second. Below the cold front, the clouds associated with wide cold frontal rainbands contain large concentrations of ice particles growing by aggregation. Above the cold front, the clouds associated with wide cold frontal rainbands are more turbulent, have more cloud liquid water, and contain embedded convective elements.

Narrow cold frontal rainbands occur at the advancing nose of the cold front, where convergence is accompanied by a narrow convective updraught a few metres per second in magnitude and a few kilometres in width. The updraught core contains young cloud characterized by high liquid water contents (0·40 to 1·40 $g\,m^{-3}$) and relatively low concentrations of small ice particles. Heavily rimed ice particles and aggregates as well as graupel also occur within the updraught. Adjacent to the updraught is found a downdraught of similar magnitude and width, but with the microphysical structure of an older cloud. Immediately outside the updraught core the ice particle concentrations are much higher than in the updraught itself, and there is much less cloud liquid water. Directly under the updraught, precipitation rates tend to be suppressed as many of the hydrometeors in the updraught are apparently suspended. The heavy rain constituting the narrow cold frontal rainband falls in a region immediately adjacent to the updraught.

The phenomenon referred to by Kreitzberg (1964) as a prefrontal surge often produces a 'surge rainband'. The prefrontal surge appears similar to a cold front aloft, above the

warm front in an occluded cyclone. The microphysical structure of the clouds associated with the surge rainband is similar to that associated with some regions of wide cold frontal rainbands, warm frontal rainbands, and older warm sector rainbands, being rather homogeneous and nearly glaciated, with ice particle concentrations in the range of 1 to 60 l^{-1}. The surge rainband is followed by a field of small convective towers extending upwards from a layer of cloud associated with the warm front below. These towers occur in various stages of development, and range from young towers, containing mostly supercooled cloud water, to old, glaciated towers, with high concentrations of ice particles. The convective towers are sometimes arranged in lines producing small, 'wavelike' rainbands, while on other occasions, the convection is more random, producing spotty showers behind the surge rainband.

Postfrontal rainbands occur in the cold air mass in the rear of the cyclone, well behind the main cold front. They can resemble organized convective systems and sometimes appear to be related to secondary cold fronts. The clouds in these rainbands have the microphysical structure of convective elements in various stages of development.

Besides having basic differences in structure, the types of mesoscale rainband which have been described have several common features. Firstly, the dynamics of each type of rainband appears to be related in some way to mesoscale frontal structure. Therefore a full understanding of these important precipitation-producing features cannot be separated from an improved understanding of the mesoscale dynamics of frontogenesis. Secondly, each type of rainband contains, in some region of its cloud, some form of cumulus-scale convection. Thirdly, each type of rainband is associated with clouds that contain high concentrations of ice particles, nearly always greater than 1 and sometimes greater than 100 per litre. Finally, collectional processes appear to be a dominant factor in the growth of precipitation particles in all the mesoscale rainbands. Aggregation tends to be the dominant mechanism in broader, often glaciated regions of high ice particle concentrations, such as are associated with warm frontal, old warm sector, wide cold frontal, and surge rainbands. Riming and sometimes the formation of graupel are important in the more strongly convective rainbands (young warm sector, narrow cold frontal, and postfrontal rainbands, and the small bands of showers behind surge rainbands). Clearly, to understand more fully the mechanisms by which precipitation forms in mesoscale rainbands within extratropical cyclones, the microphysics of the ice phase, including aggregation, must be accounted for and modelled accurately.

Research aimed at understanding the interrelationships of dynamical and microphysical processes as they are organized on the mesoscale in extratropical cyclones is of fundamental interest, since it is in the domain of dynamical–microphysical interrelationships that we anticipate significant advances to be made in understanding precipitation mechanisms (Mason 1969), and, in the case of extratropical cyclonic storms, it is on the mesoscale, specifically in the rainbands, that these processes produce the greatest amounts of precipitation. Besides being of purely scientific import, this work also appears to have potential practical applications in several areas. For example, the conceptual models of cyclonic rainbands represented horizontally in Fig. 1 and vertically in Figs. 5, 7, 8 and 13, can be valuable aids in identifying mesoscale storm features on radar in short-range forecasting. They can also serve as prototypes to test the reality of the mesoscale features simulated in numerical models. Finally, information of the type presented in this paper can be used to guide the formulation of weather modification hypotheses.

Acknowledgments

We wish to thank all the members of the University of Washington's Cloud Physics

Group who helped in this research, in particular, Dr L. F. Radke, who was Flight Scientist aboard the B-23 aircraft. Thanks are also due to members of the NCAR'S Field Aviation Facility, who operated the CP-3 radar, and of the NCAR's Research Aviation Facility, who operated the Sabreliner. NCAR is supported by the National Science Foundation (NSF).

Principal support for the CYCLES project was provided by the Atmospheric Research Section of NSF (Grants ATM74—14726—A02 and ATM77–01344). Additional support was provided by the Air Force Office of Scientific Research (Contract F49620–77–C–0057), the Environmental Research Laboratories of the National Oceanic and Atmospheric Administration (Grants 04–7–022–4423 and 44033), and the US Army Research Office (DAAG29–79–G–0005).

This paper is contribution no. 491 of the Department of Atmospheric Sciences at the University of Washington.

References

Austin, P. M.	1960	Microstructure of storms as described by quantitative radar data, *Physics of Precipitation*, H. Weickman, Ed., *Geophys. Mon.*, No. 5, Amer. Geophys. Union, 86–92.
Austin, P. M. and Houze, Jr, R. A.	1972	Analysis of the structure of precipitation patterns in New England, *J. Appl. Met.*, **11**, 926–935.
Bjerknes, J.	1919	On the structure of moving cyclones, *Geophysiske Publikationer*, **1**, No. 2.
Bjerknes, J. and Solberg, H.	1922	Life cycle of cyclones and the polar front theory of atmospheric circulation, *Ibid.*, **3**, No. 1, 3–18.
Browning, K. A.	1974	Mesoscale structure of rain systems in the British Isles, *J. Met. Soc. Japan*, **50**, 314–327.
Browning, K. A. and Harrold, T. W.	1969	Air motion and precipitation growth in a wave depression, *Quart. J. R. Met. Soc.*, **95**, 288–309.
	1970	Air motion and precipitation growth at a cold front, *Ibid.*, **96**, 369–389.
Browning, K. A. and Pardoe, C. W.	1973	Structure of low-level jet streams ahead of mid-latitutde cold fronts, *Ibid.*, **99**, 619–638.
Browning, K. A., Hardman, M. E., Harrold, T. W. and Pardoe, C. W.	1973	The structure of rainbands within a mid-latitude depression, *Ibid.*, **99**, 215–231.
Gidel, L. T.	1978	Simulation of the differences and similarities of the warm and cold surface frontogenesis, *J. Geophys. Res.*, **83**, 915–928.
Harrold, T. W.	1973	Mechanisms influencing the distribution of precipitation within baroclinic disturbances, *Quart. J. R. Met. Soc.*, **99**, 232–251.
Harrold, T. W. and Austin, P. M.	1974	The structure of precipitation systems – a review, *J. Rech. Atmos.*, **8**, 41–57.
Heymsfield, A. J.	1976	Particle size distribution measurements: An evaluation of the Knollenberg optical array probes, *Atmos. Tech.*, No. 8, 17–24.
Hobbs, P. V.	1978a	Organization and structure of clouds and precipitation on mesoscales and microscales in cyclonic storms, *Rev. Geophys. and Space Phys.*, **16**, 741–755.
	1978b	The University of Washington's CYCLES PROJECT: An Overview, *Proc. Amer. Met. Soc. Conf. on Cloud Physics and Atmos. Elec.*, Issaquah, Wash., 271–276.
Hobbs, P. V. and Biswas, K.	1979	The cellular structure of narrow cold-frontal rainbands, *Quart. J. R. Met. Soc.*, **105**, 723–727.
Hobbs, P. V. and Locatelli, J. D.	1978	Rainbands, precipitation cores and generating cells in a cyclonic storm, *J. Atmos. Sci.*, **35**, 230–241.
Hobbs, P. V., Locatelli, J. D., Matejka, T. J. and Houze, Jr, R. A.	1978	Air motions, mesoscale structure and cloud microphysics associated with a cold front, *Proc. Amer. Met. Soc. Conf. on Cloud Physics and Atmos. Elec.*, Issaquah, Wash., 277–283.

Houze, Jr, R. A.	1977	Structure and dynamics of a tropical squall-line system, *Mon. Weath. Rev.*, **105**, 1540–1567.
Houze, Jr, R. A., Hobbs, P. V., Biswas, K. R. and Davis, W. M.	1976a	Mesoscale rainbands in extratropical cyclones, *Ibid.*, **104**, 868–878.
Houze, Jr, R. A., Locatelli, J. D. and Hobbs, P. V.	1976b	Dynamics and cloud microphysics of the rainbands in an occluded frontal system, *J. Atmos. Sci.*, **33**, 1921–1936.
Houze, Jr, R. A., Hobbs, P. V., Herzegh, P. H. and Parsons, D. B.	1979	Size distributions of precipitation particles in frontal clouds, *Ibid.*, **36**, 156–162.
Knollenberg, R. G.	1970	The optical array: an alternative to scattering or extinction for airborne particle size determination, *J. Appl. Met.*, **9**, 86–103.
Kreitzberg, C. W.	1964	The structure of occlusions as determined from serial ascents and vertically-directed radar, *Rept. AFCRL*–64–26, NTIS No. AD–432007, Air Force Cambridge Research Laboratories, L. G. Hanscom Field, Mass.
Kreitzberg, C. W. and Brown, H. A.	1970	Mesoscale weather systems within an occlusion, *J. Appl. Met.*, **9**, 417–432.
Marshall, J. S.	1953	Precipitation trajectories and patterns, *J. Met.*, **10**, 25–29.
Mason, B. J.	1969	Some outstanding problems in cloud physics - the interaction of microphysical and dynamical processes, *Quart. J. R. Met. Soc.*, **95**, 449–485.
Newton, C. W.	1963	Dynamics of severe convective storms, *Met. Mon.*, **27**, 33–58.
Nozumi, Y. and Arakawa, H.	1968	Prefrontal rainbands located in the warm sector of subtropical cyclones over the ocean, *J. Geophys. Res.*, **73**, 487–492.
Plank, V. G., Atlas, D. and Paulsen, W. H.	1955	The nature and detectability of clouds and precipitation as determined by 1·25 centimeter radar, *J. Met.*, **12**, 358–377.